FRIEDRICH-SCHILLER-
UNIVERSITÄT
JENA

HI JENA

HELMHOLTZ
Helmholtz-Institut Jena

A Scintillation Particle Detector for Recombination Experiments at CRYRING@ESR

Masterarbeit

Friedrich-Schiller-Universität Jena
Physikalisch-Astronomische Fakultät
Helmholtz-Institut Jena

eingereicht von
Esther Babette Menz
geboren am 25. August 1992 in Fulda

Gutachter

1. Gutachter: Prof. Dr. rer. nat. Thomas Stöhlker

2. Gutachter: Dr. rer. nat. Michael Lestinsky

Abstract

The following work describes the implementation of a single-particle detector based on a YAP:Ce scintillation crystal at the CRYRING heavy-ion storage ring at GSI. YAP:Ce is a durable and non-hygroscopic crystal that is bakeable to a certain degree and is thus suitable for installation directly in the ultra-high vacuum of the storage ring. The photons produced by the scintillator are detected by a photomultiplier tube. The detector is located downstream from a dipole magnet and is used to detect reaction products that undergo a change of their charge-to-mass ratio in the preceding straight section of the ring which houses the electron cooler. This positioning facilitates a number of applications for the setup that include the observation of beam losses both from interaction with residual gas atoms and molecules and with electrons in the cooler section. It can also be used for future recombination studies in the cooler section, providing detailed insight into the atomic structure of highly charged ions. The detector has been assembled and installed at CRYRING and was used during two beamtimes in August and November of 2018 to test its functionality and gather first experimental data. During these tests a number of issues concerning the detector itself and the signal read-out were identified and solved and the setup demonstrated its suitability for detecting single ions even at low energies of $\sim$300 keV. Moreover for the November beamtime a data acquisition system was implemented and tested.

Zusammenfassung

Die folgende Arbeit beschreibt den Aufbau eines Detektors zum Einzel-Teilchen-Nachweis auf Basis eines YAP:Ce-Szintillationskristalls in Kombination mit einer Photomultiplier-Röhre am Schwerionenspeicherring CRYRING@ESR am GSI Helmholtzzentrum. YAP:Ce ist ein chemisch und mechanisch beständiger und nicht-hygroskopischer Kristall, der zu einem gewissen Grad ausheizbar ist und daher direkt im Ultrahochvakuum des Speicherrings eingesetzt werden kann. Der Detektor ist direkt hinter einem Dipolmagneten installiert und wird dazu genutzt, Reaktionsprodukte aus der davorliegenden Elektronenkühlersektion zu detektieren, die auf Grund ihres veränderten Ladungs-Masse-Verhältnisses am Dipolmagneten von der Orbitalbahn abweichen. Diese Positionierung erlaubt mehre Einsatzgebiete für den Detektor, darunter die Messung von Strahlverlusten durch Wechselwirkung mit Restgasatomen und -molekülen und mit Elektronen in der Kühlersektion des Rings. In der Zukunft wird die Detektorposition die Durchführung von Rekombinationsstudien in der Kühlersektion des Rings ermöglichen, die detaillierte Rückschlüsse auf die Atomstruktur hochgeladener Ionen zulassen werden. Der Detektor wurde am CRYRING installiert und während zweier Strahlzeiten im August und November 2018 eingesetzt, um die Funktionalität zu testen und erste experimentelle Daten aufzunehmen. Durch diese Tests wurden eine Reihe von Problemen sowohl mit dem Detektor selbst, als auch mit der Signalauslese identifiziert und gelöst. Die grundlegende Eignung des Aufbaus zur Detektion von einzelnen Ionen auch bei geringen Energien von $\sim$300 keV konnte demonstriert werden. Für die November-Strahlzeit wurde eine Datenerfassung implementiert und getestet.

Contents

1 Introduction

The CRYRING@ESR heavy-ion storage ring provides excellent conditions for a number of atomic and nuclear physics experiments and is also the first part of the new FAIR facility to come into operation. As part of the experimental instrumentation a number of particle detectors are either planned or already being implemented at various positions. The straight section behind the electron cooler currently houses a detector based on a channel electron multiplier and the scintillation detector described in this work.

The scintillation detector consists of a YAP:Ce (yttrium aluminium perovskite doped with cerium) crystal combined with a photomultiplier tube and is positioned directly behind the straight section that houses the electron cooler. YAP:Ce has been shown to exhibit excellent scintillation properties in terms of light yield, response time and wavelength [1]. It was chosen for this detector as it possesses mechanical and chemical properties that make it suitable for operation in ultra-high vacuum and able to withstand a significant amount of radiation and particle bombardment.

The positioning of the detector allows for it to detect reaction products from recombination experiments carried out in the electron cooler section. The CRYRING electron cooler is used to produce a cooled ion beam with a significantly reduced momentum spread. Moreover the cooler can be used as an electron target to perform high-precision spectroscopy experiments [2].

Data from recombination experiments is of interest not just for atomic physics itself but for a number of other fields as well. The level structure of the atom is influenced by e.g. QED effects such as the Lamb shift caused by vacuum energy fluctuations that are especially pronounced for the high electric field strengths that occur in highly charged ions [3] or nuclear effects like hyperfine splitting [4] and isotopic shifts [5]. The theoretical values for the energy shift are calculated using perturbation theory while experimental data can be obtained by utilizing the well-defined beam energies at an electron cooler and the wide range of ions in high charge states than can be produced by the GSI accelerator infrastructure. Successful Lamb shift experiments were conducted at ESR in the past [6]. Future experiments at CRYRING@ESR will benefit from the improved conditions in the electron cooler section, which is more compact and able to produce colder electron beams compared to the ESR cooler [2]. Dielectronic recombination and the rate at which it occurs under different conditions is of particular interest to plasma physics and the research on nuclear fusion where an ionized state of matter needs to be maintained. Likewise both

dielectronic and radiative recombination are crucial to the interpretation of astrophysical radiation that often originates from objects like nebulae and stars in which these processes occur [7].

This work describes the installation and testing of a YAP:Ce scintillation detector at CRYRING@ESR including operation during two beamtimes in August and November 2018. The setup was designed by C. Hahn and P. Pfäfflein and its suitability tested at the JULIA tandem accelerator in Jena. Their work is described in P. Pfäfflein's master's thesis [8].

Following this brief introduction Chapter 2 provides background information and theory relevant to the scintillation particle detector, its implementation at CRYRING@ESR and some of its intended applications. Chapter 3 describes the setup in detail including measurement electronics and data readout. The installation and testing of the detector and the data collected during the beamtimes is detailed in Chapter 4. As a conclusion a short discussion of the results and the future of the detector setup is provided in Chapter 5.

2 Background

This chapter gives background information on a number of subjects relevant to the scintillation particle detector and its applications. The CRYRING@ESR facility is described along with some of its intended uses as part of the FAIR project. Vacuum physics including the generation and measurement of vacuum are covered due to the relevance of excellent vacuum conditions for ion beam experiments such as those scheduled at CRYRING. As a relevant example of these experiments electron-ion recombination is discussed, followed by a description of the electron cooler, both as a beam cooling device and as an electron target for recombination. As a theoretical background for the detector itself the concept of scintillation detection, the properties of YAP:Ce as a scintillation material and the use of a photomultiplier tube for detecting the light produced in a scintillator crystal are described. The chapter concludes with a short discussion of beam lifetimes and their measurement as another application of particle detector.

2.1 The CRYRING@ESR heavy-ion storage ring

CRYRING@ESR is a small synchrotron storage ring that was formerly located at the Manne-Siegbahn-Laboratory in Stockholm, Sweden, where it was in operation between the early 1990s and 2010 before being transferred to the GSI facility in Darmstadt as an in-kind contribution to the FAIR project. CRYRING was modernized, extended and rearranged to fit the new location at Cave B of the GSI target hall. It now has a circumference of 54.17 m and consists of twelve straight sections, with 30° bending magnets each having a bending radius of 1.2 m in-between. Every second straight section contains quadrupole focusing elements, the other straight sections are used for various purposes (see Fig. 2.1): injection of highly-charged ions is possible from the entire upstream GSI accelerator facility via ESR. Ions in a low to medium charge state can be injected also from a local 300 keV/u RFQ injector beam line that makes it possible to operate the CRYRING independently from the rest the GSI facility. Injected ions may be decelerated or accelerated in the RF section and can be extracted for further use in the straight section opposite the injector. The injected beam can be cooled by electron cooling to pro-

vide narrow and monoenergetic beams that can be used for experiments in the remaining straight section. Depending on the ion energy beam lifetimes range from a few seconds up to 15 min [2]. The stored beam is monitored by beam diagnostics including destructive methods like fluorescent screens and Faraday cups and non-destructive ones like AC- and DC-transformers for beam current measurement and Schottky pickups, beam position montitors (BPM) and ionization profile monitors (IPM) for position monitoring [9].
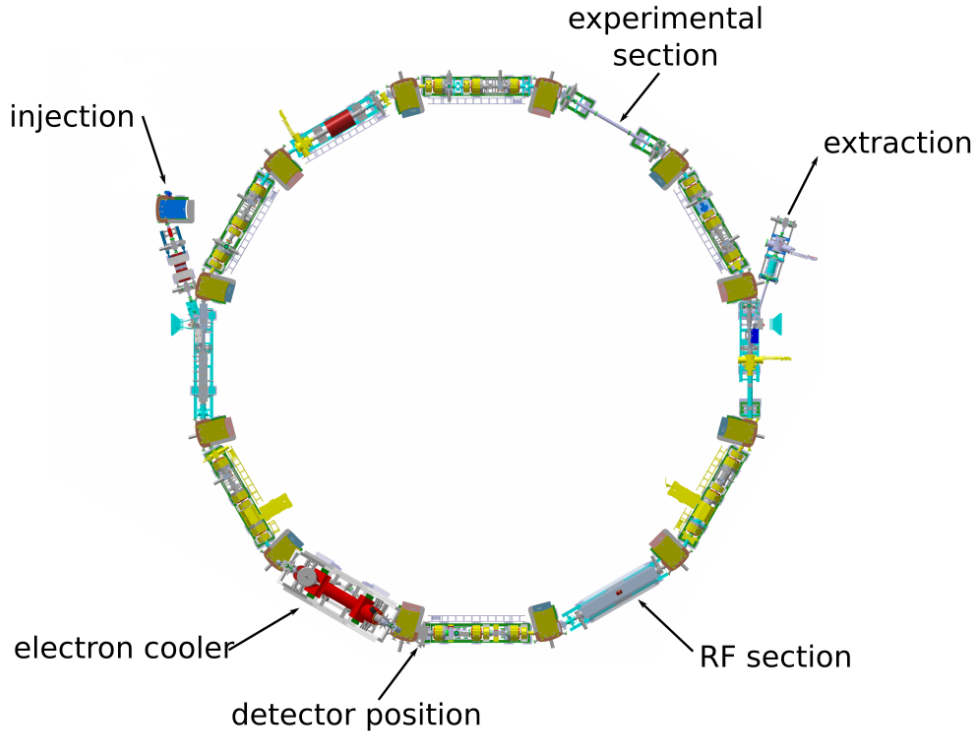

Figure 2.1: Topview of the CRYRING ion storage ring [2].

As part of the FAIR project CRYRING will operate mainly in conjunction with the Experimental Storage Ring (ESR) and will decelerate ions coming from the ESR to perform experiments at kinetic energies ranging from ∼14 Mev/u to energies lower than 300 keV. Experiments performed there will benefit from the availability of a wide range of ion beams at different charge states including the strong-field regime of heavy highly-charged ions up to bare uranium. These ions were out of reach at the Stockholm installation and are only possible in combination with ESR [2].With its fast ramping capability CRYRING@ESR is able to quickly deliver stored ions at the desired energy to experiments thus allowing for measurements on short-lived species including radioactive beams produced at the fragment separator (FRS).

Most experiments yield product ions with a higher or lower charge state than their parent

beam or even a change in mass following nuclear experiments. These reaction products separate from the orbiting beam at different angles according to the change in their charge-to-mass ratio. They are observed using a set of detectors at various positions in the straight sections directly downstream from the electron cooler and the experimental section (see Fig. 4.3).
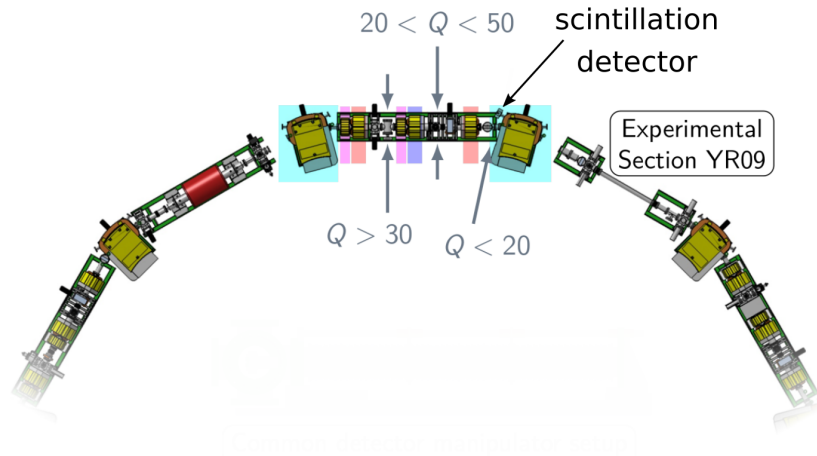

Figure 2.2: Possible positions for particle detectors in the straight section behind the experimental section. Depending on the initial charge Q of the parent beam, separation of the charge-exchanged ions from the circulationg beam is achieved at different distances downstream form the interaction site. The detector positions behind the electron cooler section are equivalent.

2.2 Vacuum physics

2.2.1 Classification of vacuum

The term vacuum (from Latin *vacuum* meaning 'not containing or holding anything', 'empty' [10]) describes any space with a pressure that is lower than the surrounding atmospheric pressure. This very broad spectrum of pressures encompasses everything from low vacuum (pressure $p \geq 1$ mbar) to extreme ultrahigh vacuum (XUHV, $p \leq 10^{-12}$ mbar) and as a result is characterised by a wide variety of physical properties and technical

applications. In accelerator physics the good vacuum conditions are indispensable as they allow accelerated particles to move freely without colliding with residual gas particles. The average length a particle can travel through a vacuum without interacting with another particle is called mean free path λ and is given by

$$\lambda = \frac{1}{\sqrt{2}n\pi d^2} \tag{2.1}$$

where d is the diameter of the particle travelling through the vacuum. The number density n, that is the number of gas particles per unit volume, is related to the pressure by

$$p = nk_BT = \frac{n_M R_0 T}{V}. \tag{2.2}$$

Here k_B is the Boltzmann constant, T the temperature, n_M is the gas quantity in moles, R_0 the universal gas constant and V the volume occupied by the gas. p is the total pressure which can be described as the sum to the partial pressures of the atomic and molecular species making up the residual gas in the vacuum chamber:

$$p = p_1 + p_2 + ... = \frac{n_{M,1}R_0 T}{V} + \frac{n_{M,2}R_0 T}{V} + ... \tag{2.3}$$

where p_i is the pressure that would be exerted by n_i moles of a gas species occupying the volume V alone [11].

Vacuum is commonly classified into several ranges (see Tab.2.1) that exhibit different physical properties, though of course the transitions are fluid. CRYRING operates at pressures of about 10^{-11} mbar which for a hydrogen molecule (H_2, d=275 pm [12]) at room temperature translates to a mean free path of about $12,000$ km. Considering the circumference of CRYRING of 54.17 m this means that a H_2^+ ion can complete an average of ca. $223,000$ revolutions without a collision. This may seem a lot until one takes into account the revolution frequency of 7 μs at an energy of 300 keV/u (the injection energy from the local source at CRYRING [2]) which means that the average time between collisions is just 1.7 s.

This simple model for the free path of stored ions in the ring does not take into account the long-range Coulomb forces exerted by ions. As the Coulomb force is proportional to the charge state of the ion, the effect on the interaction cross-section is especially pronounced for highly-charged ions. This has to be considered when calculating, e.g. electron capture cross-sections and lifetimes of stored beam as detailed in [13] and [14]. In order to achieve the storage of highly-charged ions with long lifetimes therefore, excellent vacuum conditions are necessary.

Table 2.1: Classification of vacuum [11]

	pressure [mbar]	particle density [$1/cm^3$]
low vacuum	$\sim$1000 to 1	10^{19} to 10^{17}
medium vacuum	1 to 10^{-3}	10^{17} to 10^{14}
high vacuum (HV)	10^{-3} to 10^{-8}	10^{14} to 10^{9}
ultrahigh vacuum (UHV)	10^{-8} to 10^{-12}	10^{9} to 10^{5}
extreme ultrahigh vacuum (XUHV)	10^{-12} and less	10^{5} and less

2.2.2 Generation and measurement

In order to create a vacuum the gas inside a chamber has to be removed. For low vacuum this can be done with displacement pumps that move quantities of gas from an inlet to an outlet by an interplay of valves and movable mechanical parts. Displacement pumps can operate from atmospheric pressure down to about 10^{-3} mbar. Examples include rotary vane, Roots and scroll pumps. For pressures below 10^{-3} mbar the gas can no longer be described by fluid dynamics and thus can no longer be 'sucked' towards the outside of a pump as the molecules have very little interaction with each other. Instead momentum transfer pumps are used that impart a momentum to particles entering the pump in order to propel them to the outside. These pumps can create vacua down to about 10^{-7} mbar but can not operate with their outlet at atmospheric pressure and instead require a pre-pump to create a rough vacuum. Examples of momentum transfer pumps are turbomolecular pumps and diffusion pumps. To reach UHV and beyond so-called capture pumps are used. These do not remove the gas from the vacuum chamber but bind it to surfaces by condensation or adsorption, thus removing it from the gas phase. Ion pumps and non-evaporable getter (NEG) pumps are examples of capture pumps.

Simply removing the gas inside a chamber by pumping is insufficient for achieving UHV conditions of down to 10^{-11} mbar that are necessary for ion beam storage and low-background atomic and nuclear spectroscopy. One reason for this can be the contamination of vacuum components like gasket rings and screws with grease and oils. This can be prevented by cleaning components beforehand and avoiding contamination during installation by wearing gloves. Outgassing of hydrogen from the components themselves can be avoided by using low-hydrogen annealed steal. The walls of a vacuum chamber are also typically contaminated with water and other condensates that revert back to the gaseous phase once the pressure decreases and prevent or a least delay the attainment of target pressure. This process can be accelerated by baking, that is heating the chamber to temperatures typically ranging from 120 to 300° C that are maintained for several days [15].

As good vacuum conditions are a pre-requisite of successful ion beam storage the pressure inside the ring must be monitored at all times. The measurement of vacuum faces the same challenge as vacuum creation, that is the wide range of pressures and accompanying physical properties of the gas. Thus as with pumps there must be different vacuum gauges for different pressure regions with most of them not actually measuring pressure but the number density n of the gas molecules. These gauges are usually indirect, measuring a value that depends on n, an example commonly used in UHV conditions are ionization gauges that determine n by measuring the number of gas atoms or molecules ionized by an electron beam. The response of these indirect gauges can depend on the type of gas present, e.g. inert gases will show much lower rates of ionization than reactive ones. Ionization gauges fall into two categories depending on how the electron current is produced: In the case of the hot-cathode gauge electrons are emitted from a heated filament and accelerated in an electric field. On their path from cathode to anode they ionize some the gas molecules present leading to a current of positive ions that can be measured. In cold-cathode gauges an voltage of several kV is applied between anode and cathode which accelerates existing electrons which in turn ionize gas particles [11][12].

2.2.3 Residual gas

Even for UHV conditions as can be found inside CRYRING there is still a considerable number of gas atoms and molecules left inside the vacuum chamber. For a pressure of 10^{-11} mbar there are still around one million gas particles in one cubic centimeter. This residual gas will interact with the stored beam via collisions that can lead to electron capture by the ions as well as scattering of ions out of their orbit. Both of these effects will lead to beam loss and limit the lifetime of the beam in the ring (see also Section 2.6). The total amount of residual gas can be inferred from the pressure in the ring. It can however be of interest for some applications to know the partial pressures of the gas species making up the residual gas. For this purpose residual gas analyzers (RGA) are used. There are several types of RGAs based on different physical effects but they all share the same basic operational mode: the residual gas atoms are ionized and separated by charge-to-mass ratio in a mass analyzer before being detected on a particle detector. Even though these setups do not have the high precision of mass spectrometers they give a reasonably accurate picture of the atom and molecule species left in the vacuum [11].

2.3 Recombination processes

Recombination is the process of an ion capturing a free electron and thereby reducing its charge state. As the free state of the electron is higher in potential energy than the electronic bound states in the atom, recombination is accompanied by a release of energy. In the simplest case this binding energy is emitted as a photon, a process that is called radiative recombination. If the energy is instead transferred to an electron already bound to the atom the process is called dielectronic recombination. Besides recombination ions can reduce their charge state by capturing an electron not from the free state but from another atom to which it is only lightly bound. This process is called radiative electron capture.

2.3.1 Radiative recombination

Radiative recombination (RR) is the capture of a free electron into an atomic bound state with the simultaneous emission of a photon which carries away the electron's binding energy and the kinetic energy it possessed before the collision. The reverse process is photo-ionization [16]. RR occurs in the merged electron-ion beam of electron coolers where on the one hand it leads to the loss of ions that leave the orbit at the next dipole magnet due to their changed charge-to-mass ratio. On the other hand it can be used to probe the level structure of atoms if the resulting photon emission is spectrally analyzed. Electron coolers provide excellent conditions for these kinds of experiments as both the electron and the cooled ion beams have low temperatures leading to well-defined recombination energies and in turn to narrow spectral lines in the emission spectrum. Thus even small QED corrections, e.g. Lamb shift, can be examined in RR experiments [6].

2.3.2 Dielectronic recombination

Dielectronic recombination (DR), as the name suggests, involves two electrons: a free electron (e_1) captured by the ion from the continuum and a bound electron (e_2). In contrast to radiative recombination the kinetic energy of the free electron and the binding energy that is released by its capture are not emitted as a photon but instead excite a bound electron. Because a quantized amount of energy is needed for the excitation to a higher electronic state the process of dielectronic recombination is a resonant one. As the free electron is usually captured into an unoccupied shell with high quantum number n the result is an ion or atom in a doubly excited state. The electron capture forms the first step in what is essentially a two-step process. For the second step there are two routes available. As the excited electron e_2 descends back to its previous position the released
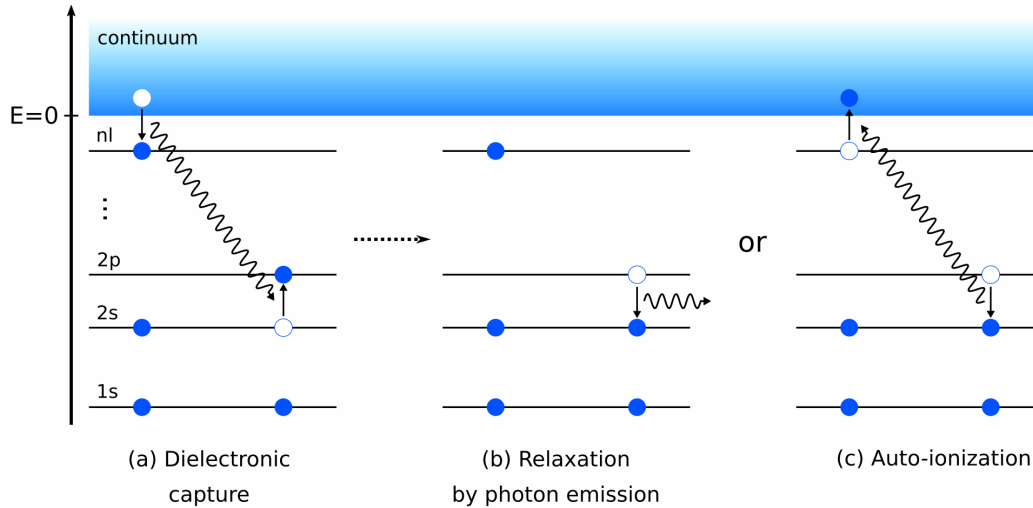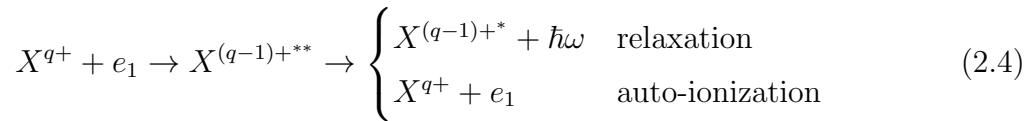
15

Figure 2.3: Dielectronic recombination: The resonant dielectronic capture **(a)** can be fol-
lowed either by relaxation via photon emission **(b)** or by auto-ionization **(c)**.

energy can be transferred back to the captured electron e_1 leading to ionization. On
the other hand the doubly excited state can also decay by emission of a photon thereby
completing the dielectronic recombination. The reverse process is the Auger effect [16].

$$X^{q+} + e_1 \rightarrow X^{(q-1)+^{**}} \rightarrow \begin{cases} X^{(q-1)+^*} + \hbar\omega & \text{relaxation} \\ X^{q+} + e_1 & \text{auto-ionization} \end{cases} \tag{2.4}$$

DR is an important process in both astrophysical and laboratory plasmas. An accurate
knowledge about the cross sections, rates and emission spectra resulting from DR is
therefore important for understanding the physics of astrophysical objects like stars and
nebulae and for controlling plasmas in fusion experiments. Another motivation for DR
experiments is the possibility to measure shifts in electronic energy levels caused by QED
effects and nuclear influences such as hyperfine splitting and isotopy effects, as the process
probes transitions between levels of very deeply bound electrons [17][2].
The precision of spectroscopic measurements of DR is limited by electron and ion beam
momentum spread as well as electron capture from residual gas atoms. Thus the ultrahigh
vacuum conditions of CRYRING and the well-controlled parameters of the electron cooler
with regard to kinetic energy of the electron and ion beams are especially well-suited [18].

2.3.3 Radiative electron capture

Radiative electron capture (REC) is a process similar to radiative recombination in that
an electron is captured by an ion followed by the emission of a photon. However in REC

the electron is captured by a highly charged heavy ion from a light ion to which it is weakly bound.

$$X^{q+} + Y \rightarrow X^{(q-1)+} + Y^+ + \hbar\omega \qquad (2.5)$$
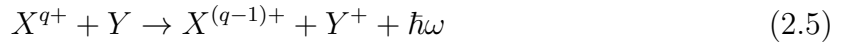
Even in a storage ring with UHV conditions there are some residual gas atoms that serve as targets for the collisions that result in REC and cause stored ions to deviate from the main orbit resulting in beam loss. On the other hand the process can be used for x-ray spectroscopy at a dedicated gas-jet target [16].
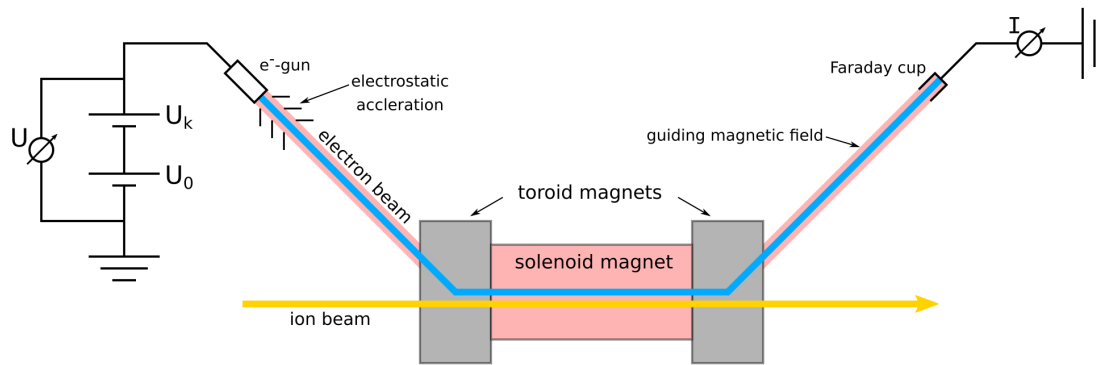
2.4 Electron cooling

Figure 2.4: Schematic set-up of the electron cooler.

2.4.1 Beam cooling

Electron cooling is employed at CRYRING to significantly reduce the circulating ion beam's momentum spread. Inside the electron cooler the 'hot' ion beam is merged with a 'cool' (i.e. of low transverse and longitudinal momentum spread) electron beam with the same average velocity. Ions that deviate from the beam velocity carry out Coulomb collisions with electrons thereby gaining or losing momentum. The result is a cooled ion beam which approximates the mean velocity and correspondingly the momentum distribution to those of the electron beam. The electron beam is produced by thermionic emission from a hot BaO-impregnated tungsten cathode as an electron gun, accelerated in an electrostatic field and collimated by ion optics. A magnetic field guides the electrons along their path which is initially at an angle to the ion beam. A toroid magnet

is used to overlay the electron with the ion beam. A solenoid magnetic field guides the beams through the interaction region before a second toroid field separates the two beams again. After separation the beam is guided into a Faraday cup where the beam current is measured [19].

A particular aspect of the CRYRING electron cooler is the use of adiabatic magnetic expansion to transversely widen the electron beam and in consequence reduce the transverse electron beam temperature. An expansion ratio of the magnetic field B of

$$\xi = \frac{B_{gun}}{B_{guide}} = 100 \tag{2.6}$$

leads to a reduction in beam temperature by $\frac{1}{\xi} = 0.01$ [20]. It should also be noted that the electron beam is longitudinally cold in relation to the stored ions though it is produced by thermionic emission. This is a result of adiabatic acceleration [21].

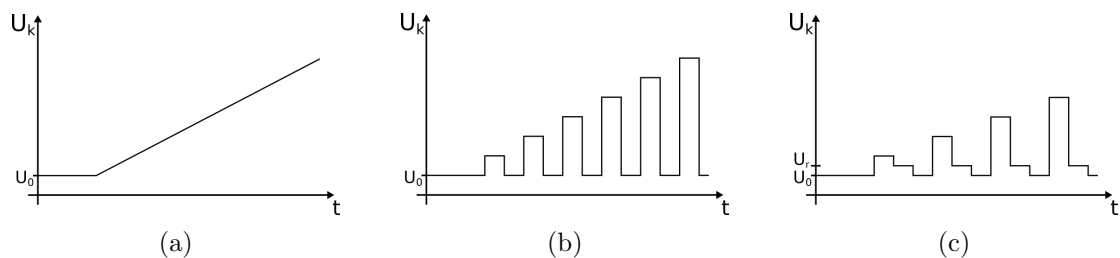### 2.4.2 Electron capture experiments

Figure 2.5: Different measurement modes for recombination experiments at the electron cooler: **(a)** continuous increase of the acceleration voltage U_k from the cooling voltage U_0, **(b)** increase of U_k in discrete steps with cooling in between and **(c)** with additional reference voltage U_r [22].

In addition to cooling the beam the electron cooler may also be used as an electron target for recombination experiments with a well-defined energy of the captured electrons relative to the ions. For this the velocity of the electron beam is systematically scanned by varying the acceleration voltage which is split into a basic voltage U_0 and a variable voltage U_k that is used for recombination experiments. This leads to a variation of the electrons' relative kinetic energy in the stored ions' centre-of-mass frame. Ions that capture electrons and thereby change their charge-to-mass ratio are separated from the main beam at the next dipole magnet and can be detected using single-particle detectors. Additionally any radiation resulting from recombination (i.e. from radiative recombination or relaxation of the doubly excited state in DR) can be detected by photon detectors installed behind the viewports at the 0° and 180° positions which provide a line of sight running through the

electron cooler. This information in combination with the velocity of the electron beam allows probing of the resonant DR process.

In order to conduct recombination measurements the acceleration voltage of the electron beam is increased above the cooling voltage U_0. The simplest way this can be done is a contiuous increase of U_k after cooling of the beam is complete (see Fig. 2.5a). This will however lead to an acceleration of the ion beam due to the cooling force of the detuned electron beam [19], an effect that is especially strong for small energy detunings and will result in energy dragging of the stored ion beam, which follows the electron energy. This problem can be mostly eliminated by increasing the acceleration voltage in discrete steps and returning to the cooling voltage after each step (see Fig. 2.5b). Additionally a reference voltage can be added after each step (see Fig. 2.5c). This is used to derive the background e.g. of reactions with residual gas. The reference voltage should therefore be chosen in such a way as to obtain a relative energy of the electron beam that is not expected to produce a DR resonance. The electron current and the acceleration voltage U_k are measured. The electron energy in the centre-of-mass frame is

$$E_0 = (\sqrt{E_e} - \sqrt{E_c})^2 \tag{2.7}$$

in the nonrelativistic limit, where E_e is the average kinetic energy of the electron beam. The cooling energy $E_c = (m_e/m_i)E_i$ depends on the target kinetic energy E_i of the ions and their mass m_i [18].

2.5 YAP:Ce scintillation detector

2.5.1 Product beam trajectories

The detection of reaction products with an altered charge state is possible because the dipole magnets that keep stored ions on their orbit are selective to the charge-to-mass ratio. The bending radius of charged particles in the magnetic dipole field is

$$r = \frac{mv}{qB}. \tag{2.8}$$

If an ion undergoes a change of charge state or a change of mass, e.g. in molecular break-up or nuclear reaction, it will have a bending radius r_p that will differ from the bending radius r_i of the stored beam:

$$r_p = \kappa r_i \tag{2.9}$$

19

where κ is relates the charge-to-mass ratio of the product particle to that of the stored ions:

$$\kappa = \frac{q_p/m_p}{q_i/m_i}. \tag{2.10}$$

Fig. 2.6 shows qualitatively some possible trajectories of reaction products directly after the magnetic dipole field where the scintillation detector described in this work is located. This positioning allows for the detection of product ions with a significantly increased bending radius r_p, e.g. light ions that captured an electron in the electron cooler section. If the bending radius is closer to that of the orbiting beam the detection takes place further down the subsequent straight section [21].
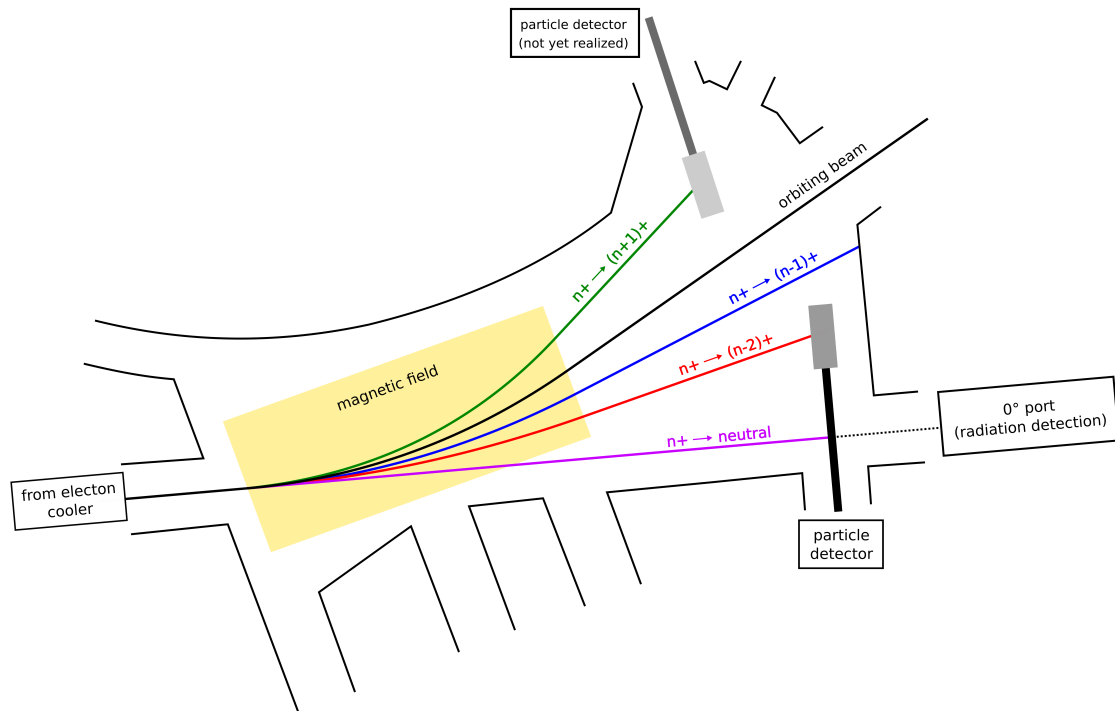

Figure 2.6: Ion trajectories after charge exchange: Ions that were stripped of an electron have a smaller, those that captured an electron a larger bending radius and can be detected by the single particle detector described in this work. Additionally the detection of radiation emitted from RR or the relaxation of the excited state in DR can be detected at the 0° port as long as it is not blocked by the detector.

2.5.2 Scintillation detection

In order to detect particles they must interact with their surroundings to eventually create a measurable electronic signal that can be recorded by a data acquisition system. In the

case of scintillation detection this happens through energy transfer from the impinging particles to the atoms of the detection material that leads to electronic excitation which subsequently decays by the emission of a photon. This process is called scintillation (from Latin *scintilla* meaning 'a particle of fire', 'a spark' [10]). The resulting photons can be detected by a photomultiplier tube. The process of electron excitation is determined by the type of scintillator material. The electrons in non-metallic inorganic scintillators are organized in a band structure with a number of completely filled bands, the energetically highest of which is called the valence band, and an empty conduction band. An ion passing through the crystal may excite electrons from the valence to the conduction band creating an electron-hole pair. As the band gap in typical inorganic crystals is in the range of 4 to 12 eV [23] de-excitation in the pure and ideal crystal would not lead to the emission of visible light. In order for the crystal to function as a scintillation material it must therefore contain luminescence centres whose band gap is smaller than that of the surrounding crystal. Luminescence centres can be formed by defects in the crystal structure or by doping the material with foreign atoms. Electron-hole pairs created by excitation can move along the band structure until they are trapped in a luminescence centre and decay back to the ground state causing the emission of visible or in the case of YAP:Ce near-UV light.
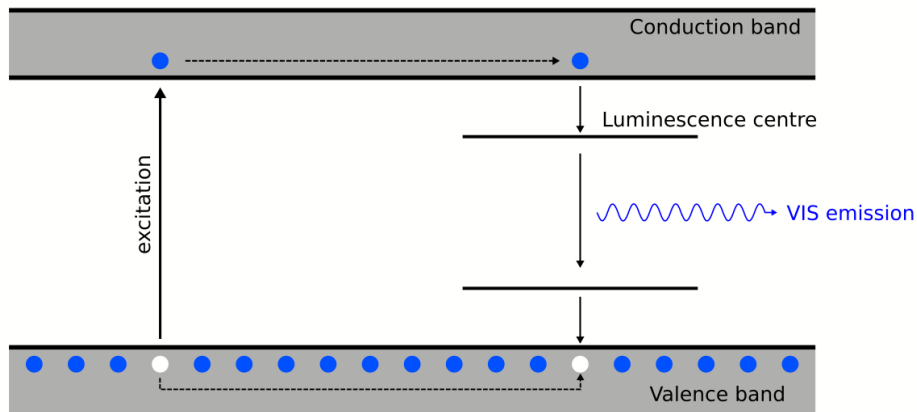

Figure 2.7: Scintillation process: An electron-hole pair is formed by excitation from the valence to the conduction band; the excited state then decays via a luminescence centre causing the emission of visible light.

2.5.3 YAP:Ce as scintillation material

The scintillation detector setup described in this work uses YAP:Ce as a scintillation material. YAP stands for yttrium aluminium perovskite, an artificial crystalline material

that is mechanically and chemically stable, non-hygroscopic and possesses similar mechanical properties as garnet [1]. The chemical formula is *YAlO$_3$* and the crystal takes the perovskite structure with yttrium in the cube-corner position $(0, 0, 0)$, aluminium in the body-centre position $(\frac{1}{2}, \frac{1}{2}, \frac{1}{2})$ and oxygen in the face-centre position $(\frac{1}{2}, \frac{1}{2}, 0)$ [24]. YAP can be activated with cerium which replaces some of the yttrium atoms in the lattice and acts as an electron donor. The activated compound exhibits scintillation properties that make is suitable for particle detection in extreme UHV. In particular the emission wavelength of 370 nm is well suited for detection with a photoelectron multiplier. The light yield is about 40% when compared to NaI:Tl, with a photon yield of 10,000 photons per MeV of deposited energy. The decay constant of 25 ns is short compared to NaI:Tl (230 ns) and YAG:Ce (70 ns) [1]. YAP:Ce has been shown to be resilient to bombardment with heavy ions, with a smaller decrease in detection efficiency compared to other set-ups, such as silicon detectors [25][8]. The fact that it is non-hygropscopic means that YAP:Ce can be exposed directly to the ring vacuum as it does not bind water that would later be released thereby compromising the ring vacuum. This eliminates the need for a vaccum window that would lead to a decrease in detection efficiency. However the exposed surfaces of the scintillation crystal are coated with a thin aluminium layer that prevents stray light from entering the detector and increases the detection efficiency by reflecting back light produced by scintillation inside the crystal.

2.5.4 Photomultiplier tube

The photons generated inside the scintillation material must in turn be detected in order to produce an electrical output signal that can be processed. For this a photomultiplier is installed behind the crystal. Despite its name a photomultiplier does not actually multiply photons but converts them into photoelectrons. The incoming photons are absorbed by a photocathode at its front end were they transfer their energy to electrons. If the photons provide sufficient energy to the electrons they are able to migrate to the material surface and leave the photocathode. These photoelectrons are then accelerated in an electrical field towards a dynode where they can cause further electrons to be emitted by secondary electron emission. This process is repeated over several dynode stages until a measurable output pulse of typically 10^6 electrons arrives at the anode.

The voltage supply to the photocathode, the dynodes and the anode is usually realized by a single high voltage that is applied to a voltage divider. In order to have the signal output at ground potential a high negative voltage is often applied to the photocathode with increasingly smaller negative voltages at the dynodes. Alternatively the photocathode can be grounded to reduce noise, in this case the anode is at high positive voltage and should be capacitively coupled to the signal output [27][28].
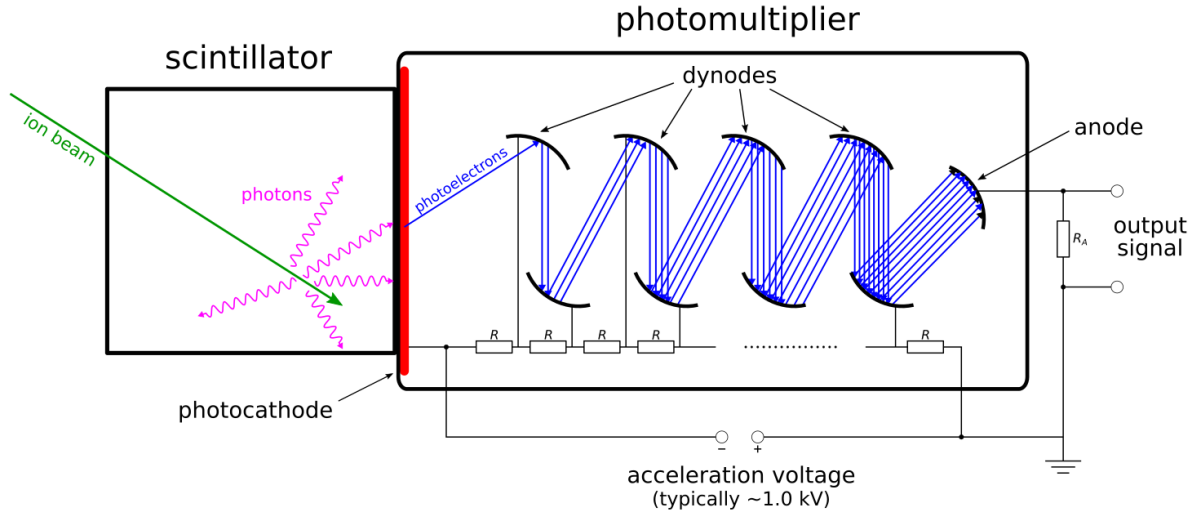
Figure 2.8: Working principle of a photomultiplier tube (drawing based on [26].

2.6 Beam lifetime measurement

Once an ion beam has been injected into the ring it has a finite lifetime due to factors like resonances of the betatron oscillation that remove ions from their orbit thus decreasing the beam current. Another important factor for beam loss is a change in charge state. Ions that capture or lose an electron in one of the straight sections of the ring (e.g. in the electron cooler) will be 'lost' at the next dipole magnet where their trajectory will deviate from the nominal beam orbit. One channel for charge exchange is the interaction of stored ions with residual gas particles. Electron cooling will also lead to some beam loss because ions do not only perform Coulomb collisions with the electrons but can also capture them via RR and DR. Conversely ions can also be ionized further e.g. by by electron impact. Using a single particle detector to count the ions that leave the beam orbit following a dipole magnet can give a measurement of the ion losses from the main beam that are caused by a change in charge state.

2.6.1 Beam lifetime

The decay of beam intensity $I(t)$ for a coasting beam, where the losses are mainly due to charge exchange with residual gas atoms and non-linear resonances, can be described approximately by an exponential decay of the form

$$I(t) = I_0 \cdot \exp\left(-\frac{t}{\tau_{beam}}\right) \tag{2.11}$$

23

where I_0 is the initial beam intensity and τ_{beam} is defined as the lifetime of the beam. The change in intensity is then

$$\frac{dI(t)}{dt} = -\frac{I_0}{\tau_{beam}} \cdot \exp\left(-\frac{t}{\tau_{beam}}\right) = -\frac{I(t)}{\tau_{beam}}. \qquad (2.12)$$

However in real conditions the lifetime is not always constant as for example the rate of residual gas collisions can change due to fluctuations in vacuum conditions [29].

2.6.2 Rate measurements

While the collisions of beam ions with residual gas atoms are a major cause of intensity decay it can also be used as a means of measuring the intensity. The products of charge exchange in one of the straight sections of a storage ring will deviate from the main orbit at the next dipole magnet and can then be measured. Assuming the number of residual gas atoms stays the same the rate of charge exchange recombinations should fall linearly with the intensity of the ion beam (see equation 2.12). The measured count rate on the detector will also include reaction products from other sources such as electron capture in the electron cooler and in the case of an H_2^+ beam molecular break-up into a proton and a neutral H atom which can also be detected. Assuming only decay channels whose rates are proportional to the intensity of the beam the measured count rate over time can be used to observe the lifetime of the beam:

$$C(t) = C_0 \cdot \exp\left(-\frac{t}{\tau_{beam}}\right) \qquad (2.13)$$

where $C_0 = C_1 + C_2 + ...$ is the sum of the of the co-efficients of the different decay channels.

3 Experimental set-up

The detection of ions in an altered charge state with a single particle detector requires the ions to be separated from the main beam. A detector performing this task in an ion storage ring must therefore be positioned on the far side of a dipole magnet from the interaction zone that produces the altered charge state. In this case electron capture takes place inside the electron cooler and the scintillation detector is positioned just behind the next downstream dipole magnet. This placement allows for the detection of ions in low charge states ($Q_{parent} < 20$) where the capture of one electron leads to a significant change in charge-to-mass ratio and therefore a significant deviation from the main beam. For the detection of ions in higher charge states there is another detector further down the subsequent straight section (see Fig. 4.3). This detector is based on a channel electron multiplier (CEM).

The parameters of CRYRING and the planned experiments in the electron cooler section placed a number of requirements on the single-particle detectors. The low possible storage energies of <300 keV made detection through a vacuum window undesirable which meant that a material suitable for UHV conditions was required for the detector head. Energy resolution was not necessary as the detector was to be operated as a particle counter. For this a good time resolution and a short deadtime were necessary to cope with high count rates. The geometry of the detector head needed to be designed in a way that would allow for it to be moved as close as possible to the primary beam without disturbing it. Similarly the detector mount had to facilitate the movement of the detector transversally to the beam. The repair or replacement of electrical components was to be possible without compromising the ring vacuum and the same, if possible, was true for the replacement of the scintillator crystal.

3.1 Scintillation detector

The detector described in this work consists of a YAP:Ce scintillation crystal, a light guide and a Hamamatsu R8619 photomultiplier tube (PMT). The properties of YAP:Ce as described in 2.5.3 allow for it to be installed in the ring vacuum and its short decay

(a) Detector head and photomultiplier tube with aluminium casing.
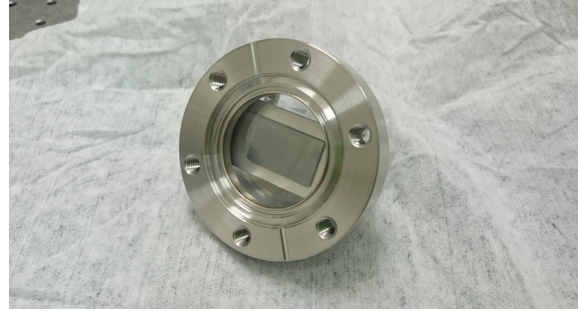
(b) Rear view of the detector head; the light guide is visible through the window flange.

Figure 3.1: Components of the detector before installation at CRYRING.

times should facilitate detection of high count rates. The crystal has a square surface of 25 mm×25 mm and a thickness of 1 mm. The square surface on one side and the four thin edges are coated with a 200 nm layer of aluminium. The wedge-shaped light guide is made of fused silica and likewise coated with aluminium on four of its six surfaces. The crystal and the light guide comprise the detector head and are mounted on the front of a window flange made of fused silica (see Fig. 3.2). This flange closes off a stainless steel tube inside of which the PMT is pressed against the window from the other side. While the detector head is exposed to the vacuum inside the ring, in order to avoid loss of detection efficiency, the PMT is outside the vacuum and can be removed from the set-up during bake-out. As the PMT is also the only electronic part of the set-up this means that no electronic feed-throughs are required and that a faulty PMT can be exchanged or repaired without breaking vacuum. The PMT is run with a negative high voltage of about -1.0 kV that is supplied by an Iseg SHQ 224M HV source meaning that the signal output is at ground potential. Both the HV source and the signal processing electronics are located on top of the CRYRING cave for easier access when the cave is closed during beam times. HV input and signal output are run through a cable patch panel into the cave where they connect to the PMT (see Fig. 3.3).

The detector is mounted inside a flexible metal bellow (see Fig. 3.2c) that sits on a travelling mount so the detector can be moved into and out of the dipole chamber. A pre-chamber that can be closed off the from the ring vacuum by a valve means that the detector head can also be accessed without the need to break the ring vacuum. This facilitates the exchange of the scintillation crystal if the detection efficiency degrades at the end of its lifetime. The scintillation crystal is pressed against the light guide by a holder that can be released by removing two screws making replacement easy [8].

(a) Half-section of the detector
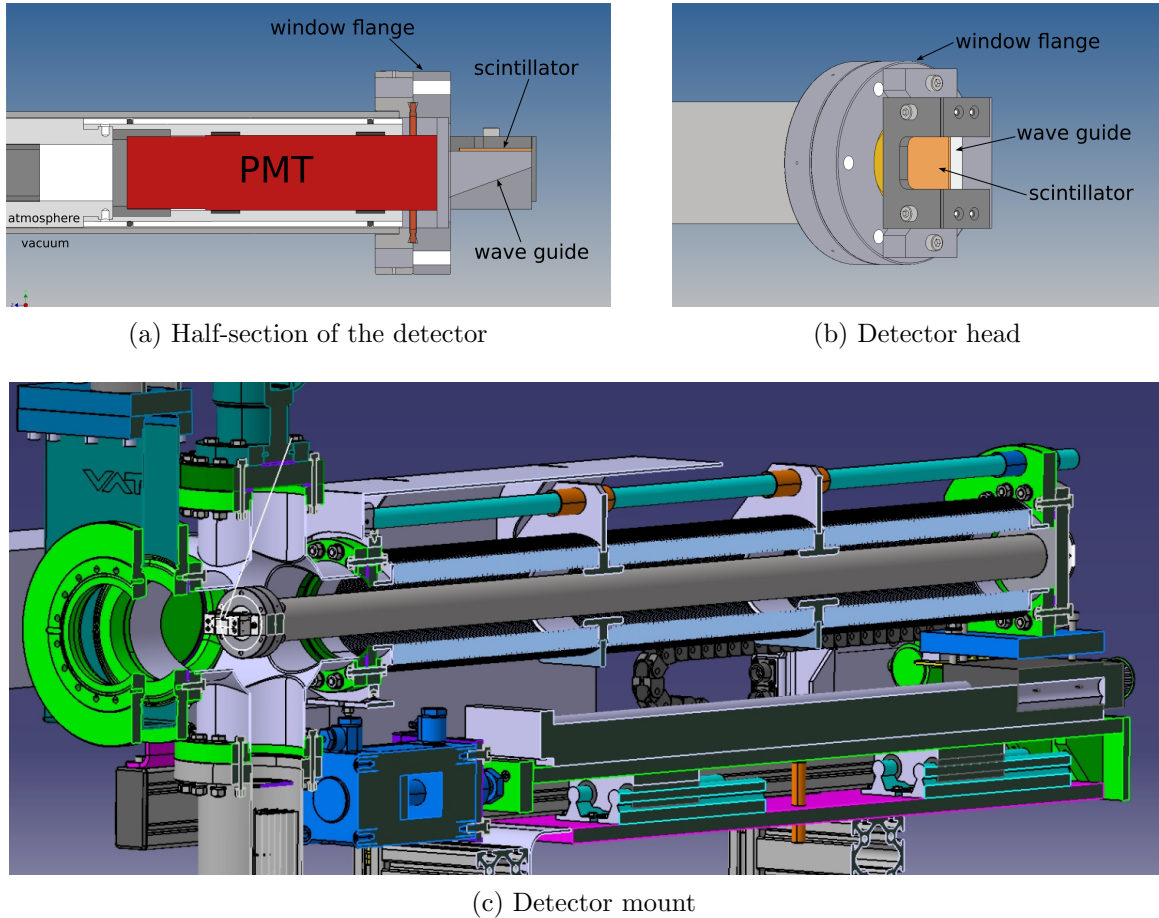
(b) Detector head

(c) Detector mount

Figure 3.2: **(a)**,**(b)** Models of the detector with the PMT (*red*) and the scintillator crystal (*orange*) [30] and **(c)** the detector inside the mount [31].

The pre-chamber is evacuated using a pre-pump and brought to high vacuum ($>\sim 10^{-8}$ mbar) using a turbomolecular pump. After bake-out an ion getter pump is used to achieve UHV conditions of down to 10^{-11} mbar after which the valve connecting the pre-chamber to the CRYRING vacuum can be opened. To avoid damaging the scintillator, bake-out temperatures are capped at 120°C.

The geometry is adapted to the requirements of the CRYRING: the face of the scintillation crystal should ideally be perpendicular to the incident beam in order to maximise detection efficiency. Additionally the detector mount is also oriented perpendicularly with regard to the ion beam in order to detect product ions with different charge state ratios q_p/q_i compared to the stored parent beam. Thus, a head-on geometry of the scintillator crystal to the photomultiplier tube is not feasible. Instead a wedge-shaped light guide is used that couples to the scintillator on one face and to the PMT on the other and directs the emitted photons from the YAP:Ce crystal to the PMT.

3.2 Data acquisition

(a) August beam time

(b) test setup
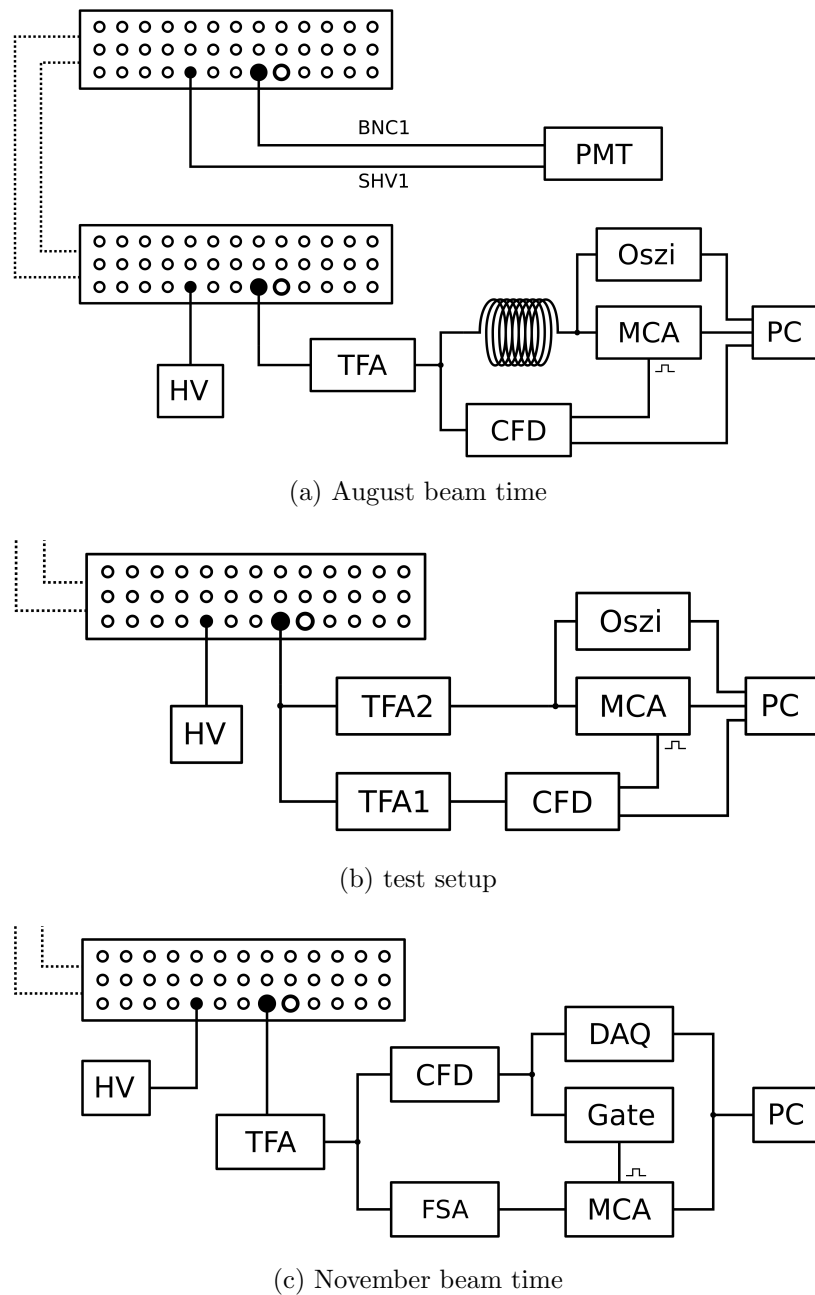

(c) November beam time

Figure 3.3: Setup of the electronic read-out equipment: The PMT is the only component that is located inside the CRYRING cave and is thus inaccessible during beam operation; the HV source and read-out electronics are located on the roof of the cave.

3.2.1 Electronics

The signal from the PMT is first amplified by an Ortec 474 Timing Filter Amplifier (TFA) that shapes the pulse for the Mesytec MCFD-16 Constant Fraction Discriminator (CFD) which converts the analogue signal into a digital pulse with a well-defined trigger time that is independent from the pulse height. The bipolar signal from the CFD provides the gate signal for the Ortec easy-mca multi-channel analyzer (MCA) which records a pulse-height distribution. As the gate preparation takes some time the signal to the MCA from the TFA was initially sent through a delay line of ∼15 m length providing about 20 ns delay so that the gate and the signal overlap at the MCA (see Fig. 3.3a). A coaxial cable shielded with aluminium foil was used as delay but this approach proved to be detrimental to signal quality due to reflections in the cable. After the first tests during the beamtime in August 2018 a different setup (see Fig. 3.3b) was tried out with a test pulse that was split to two TFAs with one (TFA1) providing an amplified signal for the CFD with an integration time of 20 ns and the other (TFA2) an amplified signal integrated over a longer time of 100 ns for the MCA. The integration leads to an increased signal length which puts the peak of the test signal inside the gate provided by the CFD. However during the November beam time it emerged that this setup did not work as expected with the real signal from the PMT as the overlap of gate and signal was not reliable. Therefore the setup was adjusted again (see Fig. 3.3c) with one of the TFAs removed and the output from the other one split to the CFD and a Tennelec TC 248 fast/slow amplifier (FSA) that provides a delayed signal to the MCA. The gate output of the CFD was processed by a GG8000 octal gate generator (OGG) to obtain a positive TTL signal that was used as a gate for the MCA. In addition the data acquistion system described in section 3.2.3 is implemented.
Both the CFD and the MCA can be controlled and read out by computer interface and the signal can at any point be observed by an oscilloscope.

3.2.2 Data acquisition with TILDA setup

Both the MCA and the CFD come with software provided by the manufacturer. In the case of the MCA this was used to acquire pulse height distributions (PHD) over a defined time period. The CFD software was used to control the parameters of discrimination, however the count rate output which had to be requested manually each time proved to be impractical for actual measurements. For the initial tests of the detector the PMT readout software of the TILDA fluorescence experiment currently running at CRYRING was used with some success. With this software both the count rate over the revolution time in the ring and over the lifetime of an injected bunch could be acquired. For the count rate over lifetime measurement the signals of a thousand bunches were summed up for
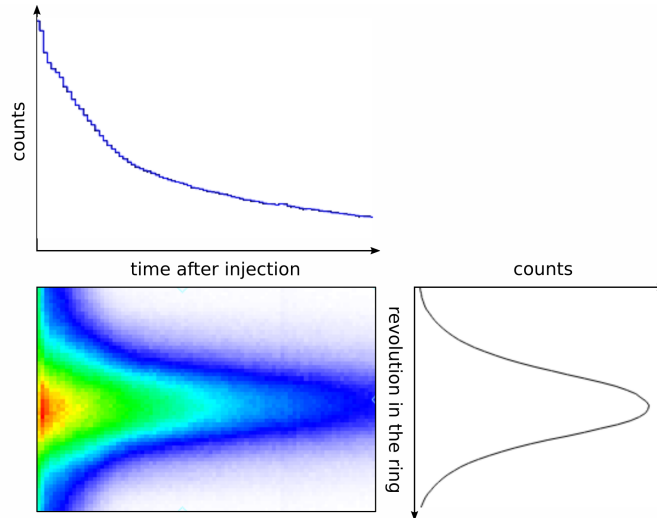
Figure 3.4: Data acquisition with the TILDA software.

one time step of 7 ms (at a revolution time of 7 μs). This read-out mode was suitable for the test beamtime in August 2018 where it showed the basic functionality of the detector and was used to measure the effects of acceleration. However the detector was built to record reaction products from the electron cooler rather than general beam-parameters and as such required a count rate read-out that can be triggered by an external event such as a change in the acceleration voltage of the electron beam in the cooler.

3.2.3 Dedicated data acquisition

A simple data acquisition system (DAQ) was implemented based on the multi-branch system (MBS; [32]) developed at GSI. The main component of the system is a scaler that is triggered by a clock generator and counts the incoming signals from the CFD between two triggers, the total count is then passed on to a RIO module. The frequency provided by the clock generator is tuneable and its adjustment should depend on the resolution required for the measurement. During the November beamtime it was set to 10 Hz resulting in a time resolution of 0.1 s. The Go4 software [33] developed at GSI is used to process the data provided by the RIO module both in real time during the experiment as well as for later analysis. For the evaluation of the detector accuracy the count rate of an ionization profile monitor (IPM) which observes the intensity of the orbiting beam by measuring the rate of residual gas ionization was also recorded with the DAQ.

4 Implementation and measurements

4.1 Commissioning of the detector at CRYRING

4.1.1 Initial problems

During the first start-up of the detector set-up at CRYRING problems emerged with regard to the electrical isolation of the PMT. In order to accelerate photo-electrons and produce a measurable electrical signal the PMT needs to be supplied with a voltage of 1 kV which is distributed over the dynode stages. The PMT was installed in the manipulator after a bake-out of the detector mount assembly and an attempt was made to supply a voltage of 1 kV. However the anode current produced by the applied voltage was significantly higher than the 0.1 mA specified in the PMT's technical data for the maximum voltage of 1.5 kV. At 400 V there was already an anode current of ∼0.15 mA and at ∼500 V the internal safety switch of the HV source triggered and cut the voltage supply. The PMT was removed to investigate the problem but no short circuit could be located and outside of the manipulator the operating voltage of 1 kV was successfully applied though an anode current of 0.38 mA measured. After mounting the PMT inside the manipulator again the inital problems recurred and there was additionally an instability in the voltage supply.

Further investigation of the problem showed up several potential sources:

- the aluminium casing that surrounds the PMT and centres it inside the manipulator tube; upon opening this it became apparent that the PMT's coating had been damaged by the casing's sharp edge revealing the metallic material underneath

- the fixation rod which presses the PMT against the window flange and guides the SHV and BNC cables for HV supply and signal output to the outside; this was constructed without regard for tolerances and fits very tightly into the back-end of the PMT causing aluminium abrasions that contaminated the setup and could potentially lead to undesirable electrical contacts

- the SHV voltage supply cable which might be put under stress in the mounted state and cause a short circuit where it is brazed to the PMT's circuit board

In order to solve the problem a new casing for the PMT from non-conducting plastic was made and the inner diameter of the back-end of the PMT casing was increased to prevent aluminium abrasions and facilitate isolation of the fixation rod with kapton foil. With these changes the operating voltage could be successfully applied though the anode current was still 0.37 mA which is higher than the average anode current of 0.1 mA specified in the PMT's data sheet. With 1 kV applied to the PMT first signals could be detected even with the detector head still inside the pre-chamber. This dark count rate was on the order of 100 Hz.

(a) Damage to the PMT from the aluminium casing.

(b) Fixation rod isolated with kapton foil to prevent short circuits.

Figure 4.1: Kapton foil was used to isolate the damaged PMT casing and the fixation rod in order to prevent short circuits when applying the operating voltage of 1 kV.

4.1.2 Start-up

After installation of the PMT as the final component the detector was moved into the dipole chamber using the travelling mount. Since the 0° and 180° viewports of the electron cooler are presently equipped with optical windows the detector head could be visually adjusted to roughly align with the 0° position from the cooler. Neutral reaction products originating in the electron cooler pass through the dipole magnet on a straight path and can be detected at this position. With an H_2^+ beam at 300 keV/u a first series of count rate measurements was taken at different horizontal positions of the detector head to locate the count rate maximum (see Fig. 4.3).
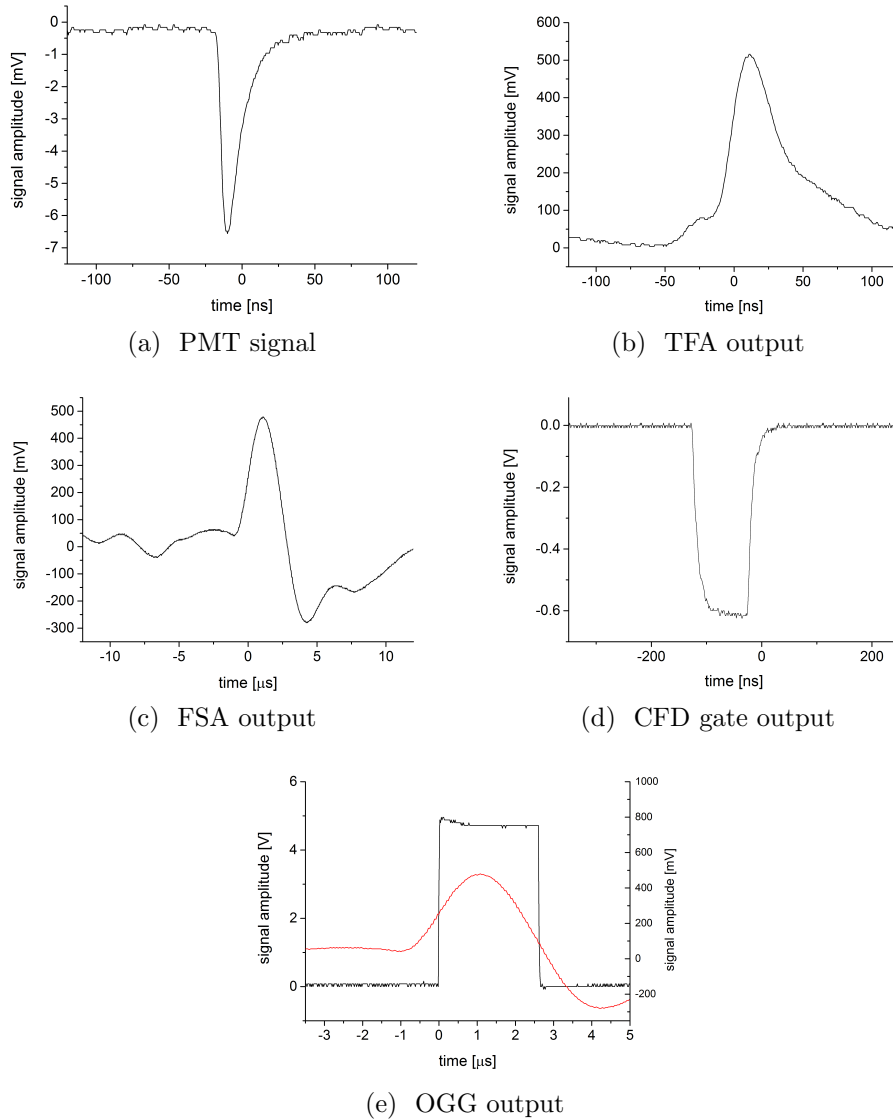
Figure 4.2: Signal shapes after the different steps of signal processing: **(a)** signal from the detector as observed in the control hut atop the cave; **(b)** pre-amplified signal from the TFA; **(c)** amplified signal from the FSA; **(d)** gate generated by the CFD; **(e)** enhanced gate from the OGG with signal from the FSA. These signal shapes are examples and do not depict the same pulse.

4.1.3 Changes and corrections after the first beamtime

The operation of the detector during a beamtime, while overall successful, showed up a number of problems with the setup. There was some difficulty in controlling the Mesytec constant fraction discriminator via the USB interface which led to uncertainty as to what parameters were actually set. A further investigation of this problem after the beamtime

showed that some of the commands did not seem to work as described in the manual. In particular the command ST 16 *val* which was supposed to set the threshold voltages of channels zero to fifteen to the same value did not seem to have any effect. Further investigation revealed that this only works if a 'common mode' is switched on. Alternatively this problem can be avoided entirely by setting the threshold individually via ST *channel val* for the input channel currently in use.

4.1.4 Output signal

The signal shapes after the various stages of the read-out as recorded by an oscilloscope are presented in Fig. 4.2. The analogue signal from the PMT has an amplitude of approximately -6.5 mV and a rise time 8 ns. It is inverted by the timing-filter amplifier and amplified to about 500 mV while the fast/slow amplifier stretches the signal to $\sim$2 μs. The fast TFA analogue signal is converted by the constant fraction discriminator to a digital NIM pulse with a length of 100 ns. This gate is then further processed by a gate generator which produces a positive TTL signal of 2.6 μs length, which is long enough to sample across the peak position of the slow amplifier's output pulse (see Fig. 4.2e).

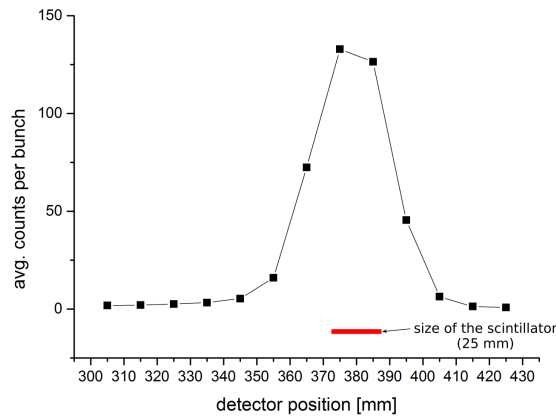## 4.2 Observation of coasting and accelerated beam

Figure 4.3: Average count rate per bunch for different positions of the detector within the dipole chamber during the August beamtime. For this measurement count rates for 86,000 bunches at each position were summed up and the average taken.

Following the successful commissioning of the setup the first measurements were taken

during the August 2018 beamtime at CRYRING. An H_2^+ beam is injected from the local source at an energy of 300 keV/u and circulated without acceleration or cooling. The count rate and pulse height spectra are recorded for a number of detector positions around the $0°$ position behind the electron cooler. The expected reactions of H_2^+ are recombination through collision with residual gas atoms leading to neutral H_2, molecular break-up of H_2^+ into a neutral H atom and a proton and a break-up of the molecule after electron capture producing two neutral H atoms. Both the H_2 molecules and the H atoms would pass the dipole magnet without being affected by the magnetic field. This would mean a peak of the count rate at the $0°$ position behind the straight section of the electron cooler. Fig. 4.3 shows the count rate for different detector positions suggesting the $0°$ position to correlate with a detector position of $\sim$380 mm however the detector position has not been calibrated. The exact peak could also not be determined as the first run of measurements took almost two hours and the beam parameters including intensity had shifted during that time due to the continued optimization and characterization measurements of the ring itself taking place in parallel. The proton resulting from the break-up has a higher charge-to-mass ratio and therefore a smaller bending radius than the parent beam of H_2^+ and cannot be detected at this detector position.

4.2.1 Rate measurements

(a) The bunch shapes for coasting and accelerated beams (the dotted lines mark the peaks).

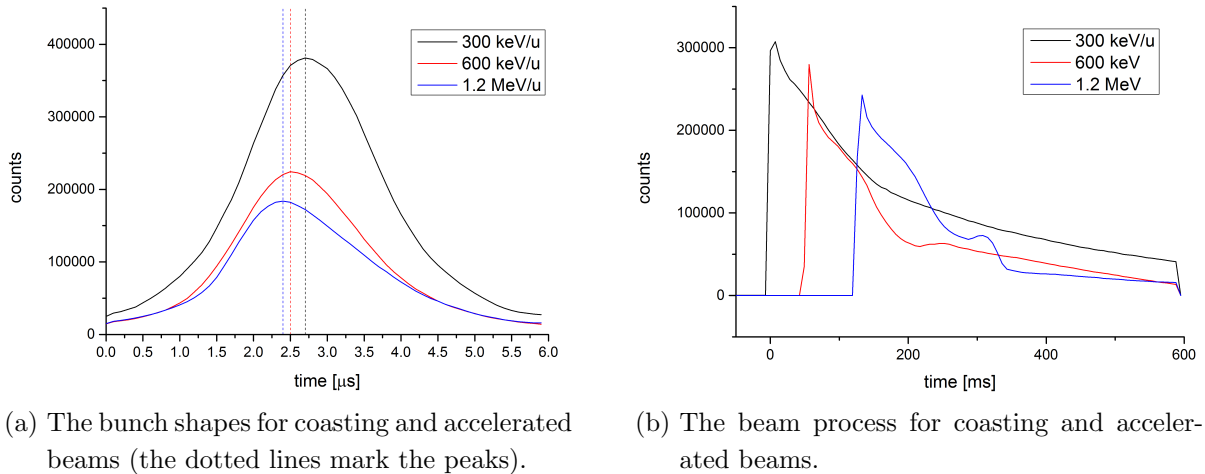(b) The beam process for coasting and accelerated beams.

Figure 4.4: Observation of the H_2^+ beam with the TILDA setup during the August beamtime.

With the data acquisition software described in Section 3.2.2 the count rate as a function of the revolution time in the ring is measured (see Fig. 4.4a). For the coasting beam the temporal bunch shape is approximately Gaussian. Once the beam is accelerated the peak

35

of the bunches is shifted to the left as the revolution time decreases. For these cases the bunch shape is no longer Gaussian but has a 'tail' because the acceleration process is included in the measurement, meaning that there are also slower bunches being measured and included in the summation. Also visible is the loss of intensity during acceleration. Fig. 4.4b shows the detector count rate for the whole beam process of the coasting and accelerated beam, the shift of the injection is due to the triggering of the measurement. The seemingly shorter duration of the beam process is an artefact caused by the shorter revolution time. This means that the time it takes to acquire the signal of a thousand bunches decreases as the beam is accelerated. Unfortunately this could not be adjusted for in plotting the data as the triggering of the measurement was too imprecise to use the ramping data of the magnets to obtain the correct revolution time. For the accelerated beams, in addition to the overall decrease in count rate, there are small peaks during the beam process that are potentially due to spatial displacement of the beam during ramping.
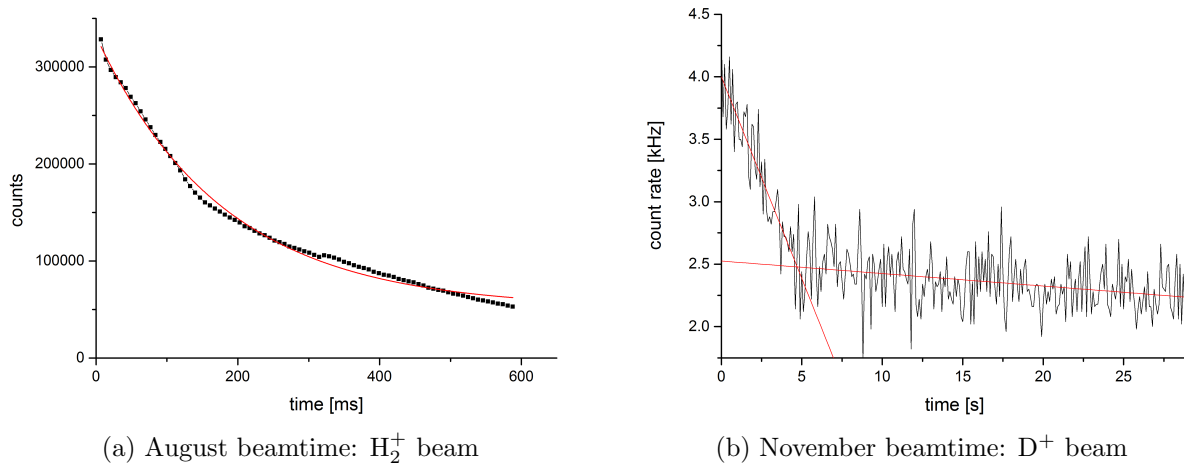

(a) August beamtime: H_2^+ beam

(b) November beamtime: D^+ beam

Figure 4.5: The measured count rate is approximated by an exponential decay (red line) to get a measure for the lifetime τ of the coasting beam. During the August beamtime the data was acquired using the TILDA setup which sums up the counts over a thousand bunches, therefore the parameter was called *counts* rather than *count rate* for the accumulated data.

The count rate over the lifetime in the ring is also measured and fitted with an exponential decay (see Fig. 4.5a) as described in Section 2.6. The fitting function is

$$C(t) = C_0 \cdot \exp\left(-\frac{t}{\tau_{beam}}\right) + C_1. \tag{4.1}$$

The results of the exponential fit are listed in Table 4.1. By this method the lifetime is determined to be $\tau_{beam}=(180.0\pm4.4)$ ms for the beamtime in August. As there are

no reliable and independent lifetime measurement for this beamtime, using other beam monitoring instrumentation, a comparison of the result is not possible. Considering the expected storage times of CRYRING of at least a few seconds the measured lifetime of 180 ms is short, which is likely a result of insufficient ring vacuum and unwanted obstructions of the beamline near the nominal beam axis by protruding cables. Prior to the November beamtime vacuum conditions were improved and the obstructions removed.

Table 4.1: August beamtime: Results of the exponential fit.

parameter	unit	value	uncertainty
τ_{beam}	ms	180.0	4.4
C_0		280,100	2,300
C_1		52,000	1,900

Table 4.2: November beamtime: Results of the linear fit.

loss process	parameter	unit	value	uncertainty
rapid initial loss	offset	kHz	4.000	0.065
	slope	kHz/s	−0.323	0.023
	τ	s	7.83	0.69
gradual loss	offset	kHz	2.525	0.035
	slope	kHz/s	−0.0100	0.0019
	τ	s	160	33

After the dedicated data acquisition system was installed a deuterium (D^+) beam was observed during the November 2018 beamtime with the electron cooling running. D^+ has a similar charge-to-mass ratio as H_2^+ but a much longer expected lifetime as molecular break-up is no longer a possible channel of beam loss. This also means that the beam loss should be easier to model. The time resolution was much coarser than in August with integration window in steps of 100 ms. The beam was injected at an energy of 291 keV and electron cooling was used to decrease the transverse and longitudinal emittance of the beam and thus improve the lifetime. There seem to be two separate regions with different rates of beam loss as evident in Fig. 4.5b. Due to the small number of data points and their high variation a simple linear fit was performed rather than an exponential fit. In this way an estimate of the time until the count rate has dropped to $\frac{1}{e}$ of the initial value was obtained for both regions of the beam loss. The first region was chosen approximately from the cooling peak (see below) to the 'bend' in the count rate, the second from there

to the end of the beam process. The results of the linear fits are given in Table 4.2. The lifetimes were estimated as (7.83±0.69) s for the first and (160±33) s for the second region of beam loss. Though it was observed on all beam diagnostic elements in the ring, the cause of the fairly rapid intial intensity decrease of the beam followed by a more steady decline could not be determined. A suspected cause of major beam loss was the radiofrequency (RF) cavity, as the amount of beam loss could be adjusted by the RF amplitude. The HF buncher which also appeared to cause a significant loss of beam was running for the whole duration of the beam process. Likewise electron cooling was applied over the whole beam process rather than just a part of it.
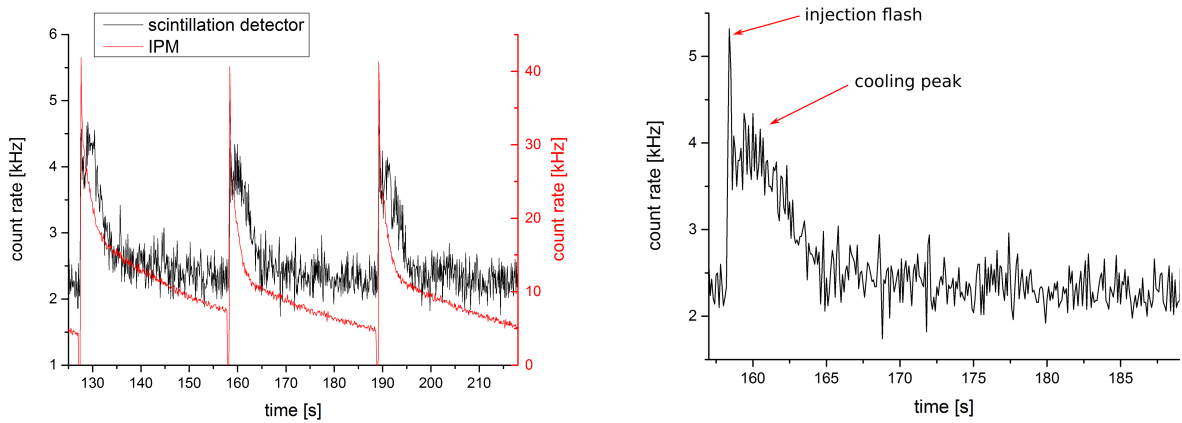
(a) The count rate measured by the scintillation detector (black) and the ionization profile monitor (red) for a cooled, coasting beam is plotted for several beam processes. Visible is the high rate at injection with the subsequent gradual loss of the beam.

(b) Details of the beam process: high count rate at the injection flash, followed by a peak caused by cooling and the subsequent loss of the beam.

Figure 4.6: Count rate measured over the whole beam process.

Fig. 4.6a shows the beam process as captured by the scintillation detector in comparison with the beam intensity data acquired by an ionization profile monitor (IPM) which observes residual gas ionization. The temporal shape of the beam process is visible with a count rate peak for injection and a decay as the beam is lost over time. However there is a dark count rate of ∼2.2 kHz at the end of the beam process and no drop to zero count rate as is present in the IPM data. While the IPM sees a single peak at injection with a subsequent decay in count rate the scintillation detector sees the initial injection flash (see Fig. 4.6b) followed by a sharp drop off and then another smaller peak. This is likely caused by the electron cooling process which leads to a rapid decrease of the stored beam diameter particularly in the beginning of the beam process. The initial beam diameter is larger than the active surface of the scintillator and some recombined particles pass by

the detector without being observed. Once the beam size shrinks due to electron cooling more particles can be detected. As this process is faster than the competing beam loss it leads to a temporary increase in count rate until virtually all reaction products from the cooler region hit the active surface of the detector.

A dark measurement was taken with the beam blocked by a Faraday cup (see Fig. 4.7) This yielded a dark count rate of (2.15±0.21) kHz which corresponds to the count rate observed at the end of the beam process. The dark signal could potentially be reduced by eliminating sources of stray light such as view ports by covering them and vacuum gauges or ionization pumps by turning them off during measurement. The effects of these measures will be investigated in a later experiment.
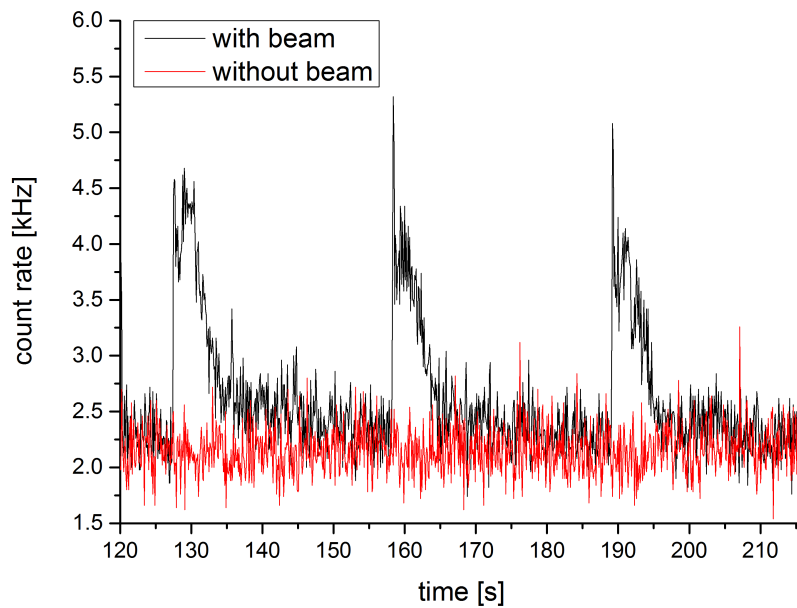

Figure 4.7: Count rate measurement with and without beam.

4.2.2 Pulse height distribution

A pulse height distribution taken for the coasting beam (Fig. 4.8) shows a distinct peak and some noise at low energies. While the production of secondary electrons in a PMT can be approximated by a Poisson model [27], a comparison of the signal peak with a Poisson distribution

$$y(x) = y_0 + exp(-\lambda) \cdot \frac{\lambda^x}{x!} \qquad (4.2)$$

where x corresponds to the channel number and y to the counts per channel, shows that the experimental data has a greater spread than is predicted in Poisson statistics. This is in accordance with literature [34] which suggests that a Pólya distribution,

39

Table 4.3: Parameters of the Poisson fit.

Parameter	Value
y_0	5.8×10^6
λ	19.5

$$P(x) = \frac{\mu^x}{x!}(1 + b\mu)^{-x-1/b} \prod_{i=1}^{x-1}(1 + ib),\qquad(4.3)$$

may be more accurate in describing the pulse height distribution produced by a photomultiplier tube. A fit of the data using the Pólya distribution was not attempted as part of this work.

Unfortunately it has so far not been possible to calibrate the MCA channels with regard to particle energy and the results are therefore only qualitative.
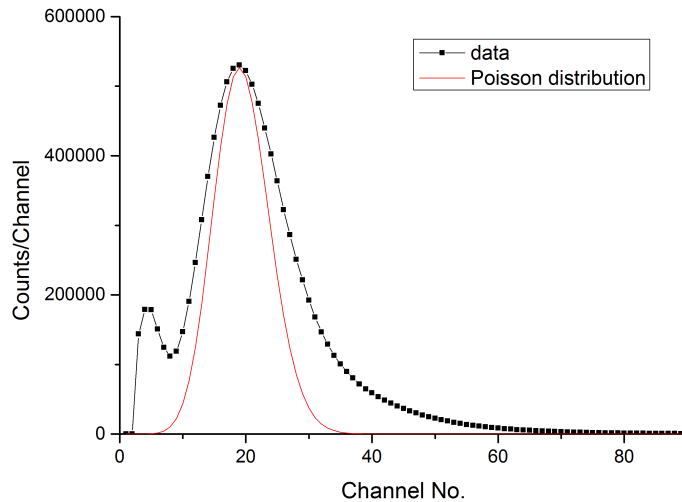
Figure 4.8: Pulse height distribution (PHD) of the PMT signal after amplification.

After acceleration of the beam is achieved the effect is clearly visible in the pulse height distribution of the signal (Fig. 4.9). Whereas the signal from the beam at injection energy (E_{beam}=300 keV/u) produces a Gaussian distribution of pulse heights, for an acceleration to 600 keV/u (red line in Fig. 4.9) there is a slight additional peak at higher channel numbers. When accelerating to an even higher energy of 1.2 MeV/u (blue line) this additional peak becomes quite pronounced. The fact that the position of the spectrum's main peak is still the same as for the unaccelerated beam is likely caused by perfoming the pulse height measurements with an electronics setup that was ungated to the ring cycle and thus included the complete process from injection at 300 keV/u through acceleration
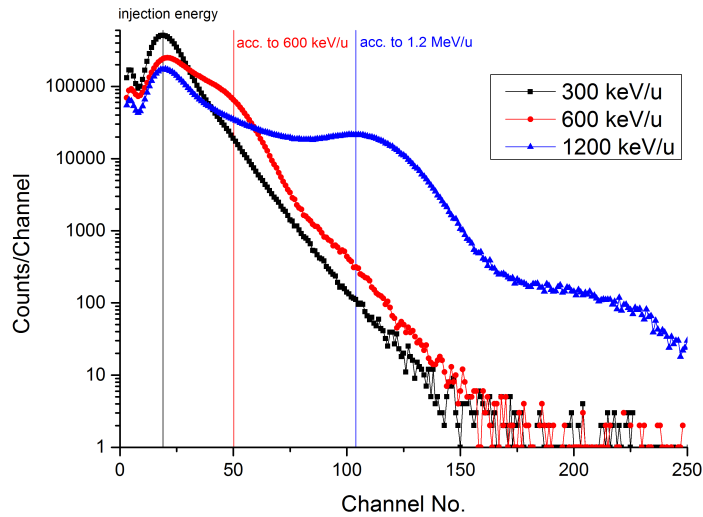
Figure 4.9: Effects of acceleration from 300 keV/u to 600 keV/u (red) and 1.2 MeV/u (blue) on the PHD.

to the measurement flat-tops at 600 keV/u and 1.2 MeV/u respectively. After the start of acceleration the intensity drops off significantly so that the signals originating from the initially coasting beam still produce a pronounced peak.

5 Discussion and Outlook

During the two beamtimes in August and November 2018 the basic functionality of the detector could be established through observation of the beam process and of the effects of acceleration and by measurements of the beam lifetimes with and without cooling. It has been shown that particle detection with the YAP:Ce crystal works even for very light ions like H_2^+ and D^+ at low energies of only 300 keV/u. A data acquisition system has been implemented and used during the November beamtime. While this is a fairly simple setup it fulfilled its function and can be used as a groundwork to build a more advanced DAQ for future experiments that takes into account additional data and ring parameters and is triggered to the beam process.

In addition to these successes a number of issues and questions still persist. The source of the high dark count and the intermittent high background count rate that were observed in November has to be investigated and – if possible – removed. An obvious approach is the methodical elimination of light sources, e.g. vacuum gauges, ionization pumps or insufficiently covered view ports, to see whether this has any effect. For the signal processing electronics multiple configurations were tried, the last of which during a running beamtime. In order to ensure a reliable and clean signal some further calibration and optimization are required. This might also help in decreasing the dark count. Calibration is also necessary for the position of the detector within the dipole chamber which has so far only been estimated.

In the next few years several experiments involving the electron cooler are planned at CRYRING@ESR. Once the ESR storage ring is in operation again, all ion species available at the UNILAC linear accelerator can be transported to CRYRING. This will facilitate recombination experiments on heavy ions in high charge states, such as Lamb shift and dielectronic recombination. In the case of the Lamb shift experiment an x-ray detector will be used for precise spectroscopy of the 1s Lamb shift and the scintillation detector can be used to provide a coincidence measurement. However as the detector blocks the 0° viewport this is only possible if the detector is moved to another position further down the straight section. Dielectronic recombination experiments will be carried out as described in Section 2.4.2. Whether the detector will be used at the present or another position depends on the kind of ions under investigation.

List of Figures

Bibliography

[1] S. Baccaro et al. 'Scintillation Properties of YAP:Ce'. In: *Nuclear Instruments and Methods in Physics Research A* 361.1-2 (1995), pp. 209–215. DOI: `10.1016/0168-9002(95)00016-X`.

[2] M. Lestinsky, Y. Litvinov, and Th. Stöhlker. 'Physics Book: CRYRING@ESR'. In: *Eur. Phys. J. Special Topics* 225.5 (2016), pp. 797–882. DOI: `10.1140/epjst/e2016-02643-6`.

[3] B. H. Bransden and C. J. Joachain. *Physics of Atoms and Molecules*. 2nd. Harlow: Pearson Education, 2003.

[4] M. Lestinsky et al. 'Screened Radiative Corrections from Hyperfine-Split Dielectronic Resonances in Lithiumlike Scandium'. In: *Phys. Rev. Lett.* 100 (2008). DOI: `10.1103/PhysRevLett.100.033001`.

[5] C. Brandau et al. 'Isotope Shift in the Dielectronic Recombination of Three-Electron ^{A}Nd^{57+}'. In: *Phys. Rev. Lett.* 100 (2008). DOI: `10.1103/PhysRevLett.100.073201`.

[6] A. Gumberidze et al. 'Quantum Electrodynamics in Strong Electric Fields: The Ground-State Lamb Shift in Hydrogenlike Uranium'. In: *Phys. Ref. Lett.* 94 (2005). DOI: `10.1103/PhysRevLett.94.223001`.

[7] S. Schippers et al. 'Dielectronic recombination data for astrophysical applications: plasma rate-coefficients for Fe^{q+} (q=7-10, 13-22) and Ni^{25+} ions from storage-ring experiments'. In: *Int. Rev. Atom. Mol. Phys.* 1.2 (2010), pp. 109–121.

[8] Philip Pfäfflein. 'Entwicklung und Aufbau eines Teilchendetektors für erste Experimente am Ionenspeicherring CRYRING.(German)'. master thesis. Friedrich-Schiller-Universität Jena, 2017.

[9] H. Danared et al. *Low-energy Storage Ring – Technical Design Report.* `https://fair-center.eu/fileadmin/fair/publications_exp/DesignReportLSR_1.3.pdf`(accessed 16 December 2018). Manne Siegbahn Laboratory (Stockholm University), 2011.

[10] P. G. W. Glare (Ed.) *Oxford Latin Dictionary.* Oxford: Oxford University Press, 2012.

[11] A. Chambers. *Modern Vacuum Physics.* London: Chapman & Hall/CRC, 2005.

[12] J. M. Lafferty. *Foundations of Vacuum Science and Technology*. New York: Wiley & Sons, 1998.

[13] I. Yu. Tolstikhina and V. P. Shevelko. 'Influence of atomic processes on charge states and fractions of fast heavy ions passing through gaseous, solid, and plasma targets'. In: *Phys.-Usp* 61 (2018). DOI: 10.3367/UFNe.2017.02.038071.

[14] V. P. Shevelko et al. 'Charge-changing processes in collisions of heavy many-electron ions with neutral atoms'. In: *Nucl. Instr. Methods B* 269 (2011), pp. 1455–1463. DOI: 10.1016/j.nimb.2011.03.024.

[15] *The Vaccum Technology Book (Volume 2)*. https://www.pfeiffer-vacuum.com/filepool/File/Vacuum-Technology-Book/Vacuum-Technology-Book-II-Part-2.pdf?referer=1456&request_locale=en_US (accessed 16 December 2018). Pfeiffer Vacuum GmbH, 2013.

[16] H.F. Beyer, H.-J. Kluge, and V.P. Shevelko. *X-Ray Radiation of Highly Charged Ions*. Berlin; Heidelberg: Springer, 1997.

[17] G. W. F. Drake (Ed.) *Handbook of Atomic, Molecular and Optical Physics*. Berlin; Heidelberg: Springer, 2006.

[18] G. Kilgus et al. 'High-resolution measurement of dielectronic recombination of lithiumlike Cu^{26+}'. In: *Phys. Rev. A* 46.9 (1992), pp. 5730–5740. DOI: 10.1103/PhysRevA.46.5730.

[19] H. Poth. 'Electron Cooling: Theory, Experiment, Application'. In: *Physics Reports (Review Section of Physics Letters)* 196.3 - 4 (1990), pp. 135–297. DOI: 10.1016/0370-1573(90)90040-9.

[20] H. Danared. 'Fast electron cooling with a magnetically expanded electron beam'. In: *Nucl. Instr. Methods A* 335 (1993), pp. 397–401. DOI: 10.1016/0168-9002(93)91223-A.

[21] Michael Lestinsky. 'High-Resolution Electron Collision Spectroscopy with Multi-charged Ions in Merged Beams'. PhD thesis. Ruperto-Carola University of Heidelberg, 2007.

[22] Michael Lestinsky. private communication. 2018.

[23] H. Kolanoski and N. Wermes. *Teilchendetektoren: Grundlagen und Anwendungen. (German) [Particle Detectors: Basics and Applications]*. Berlin; Heidelberg: Springer Spektrum, 2006.

[24] N. W. Ashcroft and N. D. Mermin. *Solid State Physics*. Philadelphia: CBS Publishing, 1976.

[25]   W. Klamra et al. 'Fast inorganic scintillators in extreme ultra high vacuum applications'. In: *Nuclear Science Symposium Conference Record*. Vol. 1. 2001. DOI: `10.1109/NSSMIC.2001.1008473`.

[26]   JKrieger. *Photomultiplier*. `https://upload.wikimedia.org/wikipedia/commons/a/ab/Photomultiplier_schema_de.png?uselang=de`(accessed 16 December 2018). Wikimedia Commons, 2007.

[27]   G. F. Knoll. *Radiation Detection and Measurement*. New York: Wiley & Sons, 2000.

[28]   *Photomultiplier Tube R8619*. `https://www.hamamatsu.com/resources/pdf/etd/R8619_TPMH1331E.pdf`(accessed 1 November 2018). Data sheet. 2014.

[29]   K. Wille. *The physics of particle accelerators: an introduction*. Oxford: Oxford University Press, 2009.

[30]   Philip Pfäfflein. private communication. 2017.

[31]   M. Lestinsky et al. *Technical Design Report: Experimental Instrumentation of CRYRING@ESR*. `https://fair-center.eu/fileadmin/fair/publications_exp/TDR_CRYRING_Experimental_Instrumentation.pdf`(accessed 15 December 2018). SPARC Collaboration, 2016.

[32]   J. Adamczewski and N. Kurz. *GSI Multi-Branch System User Manual*. `https://www.gsi.de/fileadmin/EE/MBS/gm_mbs_c_63.pdf`(accessed 03 December 2018). Gesellschaft für Schwerionenforschung mbH, 2017.

[33]   J. Adamczewski-Musch et al. *The Go4 Analysis Framework. Introduction V5.2*. `http://web-docs.gsi.de/~go4/go4V05/manuals/Go4introV5.pdf`(accessed 20 November 2018). Gesellschaft für Schwerionenforschung mbH, 2017.

[34]   J.R. Prescott. 'A statistical model for photomultiplier single-electron statistics'. In: *Nucl. Instrum. Meth.* 39 (1966), pp. 173–179. DOI: `10.1016/0029-554X(66)90059-0`.

Danksagung

Zum Abschluss möchte ich denen meinen herzlichen Dank aussprechen, durch die die Anfertigung dieser Arbeit erst möglich wurde und die mich während der, manchmal anstrengenden, Zeit unterstützt haben:

- Prof. Dr. Thomas Stöhlker, für die Vergabe des Themas, die herzliche Aufnahme in die Arbeitsgruppe und die Ermöglichung der experimentellen Arbeit in Darmstadt,

- Dr. Michael Lestinsky und Christoph Hahn M.Sc., denen ich für die geduldige und umfassende Betreuung in allen Abschnitten und Aspekten meiner Arbeit besonders dankbar bin,

- Dr. Anton Kalinin und Dr. Uwe Spillmann, die beim Aufbau des Detektors und der Auswerte-Elektronik wertvolle Hilfe geleistet haben, Felix Kröger M.Sc., der die Datenaufnahme konzipiert hat und Philip Pfäfflein M.Sc., der den Detektor konzipiert und die ersten Tests durchgeführt hat,

- Dr. Frank Herfurth und Dr. Zoran Andelkovic, für ihre Unterstützung während der Strahlzeiten und Konstantin Mohr M.Sc., der die Datenaufnahme im August ermöglicht hat,

- die gesamte Arbeitsgruppe Atomphysik hochgeladener Ionen am Helmholtz-Institut Jena und die Abteilung Atomphysik an der GSI in Darmstadt, für die nette Aufnahme, Unterstützung und willkommene Ablenkung zum richtigen Zeitpunkt,

- die Mechanische Werkstatt der GSI unter der Leitung von Herrn Romig, ohne deren schnelle und unbürokratische Hilfe die Strahlzeit im August weit weniger erfolgreich verlaufen wäre

- und natürlich meinen Eltern und meiner gesamten Familie, die mir das Studium ermöglicht und mich immer unterstützt haben.

Erklärung

Ich erkläre hiermit, dass ich die vorliegende Arbeit selbständig verfasst habe und keine anderen als die angegebenen Quellen und Hilfsmittel - insbesondere keine im Quellenverzeichnis nicht genannten Internetquellen - verwendet habe. Ich versichere weiterhin, dass ich diese Arbeit nicht im Rahmen eines anderen Prüfungsverfahrens eingereicht habe.

Mit der Veröffentlichung der Masterarbeit bin ich einverstanden.

Jena, 21. Dezember 2018

_____

Esther B. Menz